Eur. Phys. J. E (2017) **40**: 5
DOI 10.1140/epje/i2017-11490-y

THE EUROPEAN PHYSICAL JOURNAL E

Regular Article

Structural and cooperative length scales in polymer gels

Baudouin Géraud, Loren Jørgensen, Christophe Ybert, Hélène Delanoë-Ayari, and Catherine Barentin[a]

Univ Lyon, Université Claude Bernard Lyon 1, CNRS, Institut Lumière Matière, F-69622 VILLEURBANNE, France

Received 18 July 2016 and Received in final form 24 November 2016
Published online: 19 January 2017 –

Abstract. Understanding the relationship between the material structural details, the geometrical confining constraints, the local dynamical events and the global rheological response is at the core of present investigations on complex fluid properties. In the present article, this problem is addressed on a model yield stress fluid made of highly entangled polymer gels of Carbopol which follows at the macroscopic scale the well-known Herschel-Bulkley rheological law. First, performing local rheology measurements up to high shear rates ($\dot{\gamma} \geq 10^2\,\mathrm{s}^{-1}$) and under confinement, we evidence unambiguously the breakdown of bulk rheology associated with cooperative processes under flow. Moreover, we show that these behaviors are fully captured with a unique cooperativity length ξ over the whole range of experimental conditions. Second, we introduce an original optical microscopy method to access structural properties of the entangled polymer gel in the direct space. Performing image correlation spectroscopy of fluorophore-loaded gels, the characteristic size D of carbopol gels microstructure is determined as a function of preparation protocol. Combining both dynamical and structural information shows that the measured cooperative length ξ corresponds to 2–5 times the underlying structural size D, thus providing a strong grounding to the "Shear Transformation Zones" modeling approach.

1 Introduction

"Yield Stress Fluids" (YSF) such as foams, granular pastes, concentrated emulsions or polymer gels exhibit interesting rheological properties at the origin of their wide use both in the daily life and in many industrial processes [1]. Indeed, YSF share the peculiar ability to behave either as solid or liquid depending on the applied shear stress: below a critical yield stress, σ_Y, they deform as an elastic solid while they flow above σ_Y.

From a microscopic point of view, YSF are out-of-equilibrium systems made of interacting particles (bubbles, grains, droplets or polymer blobs). These particles are jammed in a disordered, glassy structure so that these materials are known to exhibit ageing [2–4] and complex rheological behaviors [5–7]. Characterizing the microstructure of YSF and the interaction between particles is of great importance to understand their rheology, the wall slip [8] or the confinement effects [9, 10], which are often encountered in applications such as coating, extrusion or soil remediation [11–13]. The knowledge of the microstructure is also of prior interest in the study of the fluidization process. In particular it has been shown theoretically [14–17] and experimentally [18,19] that the fluidization of such materials occurs through a succession of local dissipative rearrangements called "Shear Transformation Zone" (STZ) whose size is directly linked to the YSF microstructure. Indeed STZ involves typically a few tens of particles with a spatial extension of a few particle radii. Note that a certain variability on the STZ sizes in dense emulsions has been reported going from one particle radius [20] up to 20 radii [4]. The influence of shear rate on the spatial extension of STZ has also been addressed. Depending on the amorphous systems, two behaviors have been reported: the STZ size decreases as a power law of the shear rate [16, 17, 19, 21–23], or it is constant [20, 24].

An important feature of YSF flows, resulting from the Shear Transformation Zones, is their strongly cooperative and their spatially heterogeneous properties. Indeed each plastic rearrangement induces both a stress relaxation at the location of the rearrangement but simultaneously a stress redistribution (increase) in the neighborhood, which is responsible for new plastic events. This elastic stress redistribution is at the origin of the strong correlation between successive plastic events. The cooperative nature of the flows has been evidenced with various materials: granulars [25,26], dense emulsions [9], foams [3,27–30] and recently polymer gels [10]. In particular, experiments performed in confined microchannels [9] have shown that the rate of plastic events, also called fluidity, not only depends on the local stress but also on the fluidity in its surrounding due to the cooperative nature of the flow. Fluidity is then correlated on a cooperative length ξ which corresponds to the spatial extent of the plastic rearrangements.

Despite some recent successes, the generality of the STZ approach for yield stress fluids with different un-

[a] e-mail: catherine.barentin@univ-lyon1.fr

derlying microscopic structures is still the subject of debates [9, 31]. Therefore the deeper understanding of the relationship between the microscopic structural details, the geometrical confining constraints, the local dynamical events and the global rheological response more and more deserves combined experimental approaches yielding information on dynamical and structural features. This is the purpose of the present article to experimentally investigate these different aspects on a model polymer gel of Carbopol. Carbopol gels are used in many industrial processes (cosmetic, soil re-mediation) [13, 32], and also widely studied for their rheological properties [33,34]. They belong to the class of simple yield stress fluids [35] and are composed of jammed entangled polymer blobs. Compared to other microgels such as pNipam previously studied [21, 31], Carbopol gels are much more entangled and soft[1]. Studying the link between confined dynamics and structure in the case of a highly entangled polymer gels will therefore bring new insights in the general framework of the rheology and the fluidization of soft glassy materials.

In the first section of this article, we characterize the dynamical properties of Carbopol gels through bulk rheology and confined-geometry flow profiles. Velocity profiles of Carbopol gels in micro-channels were already reported by some of the authors in a previous study [10]. Here however, we push the analysis by extracting local rheology up to high shear rates. First, this allows us to confirm unambiguously the failure of bulk rheology together with the non-uniqueness of rheological properties. Along lines presented in [10], non-locality is analyzed in terms of fluidity-based models [9, 19] to extract a unique cooperativity length ξ throughout experimental conditions. Second, this analysis evidences that non-local effects manifest at high-enough shear rates, thus providing rationalization for some of the studies that missed confinement effects.

In a second section this dynamical characterization is complemented by the analysis of the Carbopol microstructure and the link between both aspects. Carbopol structure has been the object of few studies so far due to the difficulties arising from the appealing feature of very high gel transparency. Lee *et al.* [36] performed light scattering at small angles and measured a length scale of a few microns associated to the polymer blob size. However they also showed that the characteristic length of the structure is sensitive to the polymer concentration, the preparation protocol, the *p*H [36]. Thus, it is crucial to perform structural analysis on gels matching the very same preparation protocol as for the dynamical studies. In the following we introduce an original confocal microscopy approach using a fluorescent-labeling method inspired from Gutowski *et al.* [37]. Using Image Correlation Spectroscopy (ICS), the polymer gel microstructure size[2] D is determined for different gel samples. This eventually allows to establish a precise comparison between cooperativity length ξ and microstructure size D, and to discuss it in regards of the theoretical description of these systems and of other soft glassy materials.

2 Confined flows

We start here by probing the dynamical properties of Carbopol gels, with particular emphasis put to confined geometries, *i.e.*, to flow through narrow micro channel, from which cooperative effects and breakdown of a unique material rheology can be investigated.

2.1 Materials and methods

Sample preparation

Carbopol ETD 2050 powder is dissolved in deionized water heated to 50 °C. Typically the polymer weight concentration C ranges from 0.2 %wt to 2 %wt. The solution is mixed by a magnetic stirrer during 30 minutes, to equilibrate to room temperature. The solution is then neutralized with sodium hydroxyde ($\approx$ 0.5 mL NaOH, 10 M in 100 ml for $c = 0.5$ %wt) so that the *p*H rises from 3 to 7 ± 0.5. The solution is mixed by hand for homogenization and jams during this neutralization stage. The samples are then stirred by a mixer (RW20, Ika, tip: R1303) at a high stirring rate of 2100 rpm during 24 hours. The stirring is supposed to break the biggest blobs and to yield a more homogeneous structure[3]. Finally the samples are centrifuged at 3200 rpm during 10 min to remove air bubbles trapped in the bulk.

Because of the Carbopol gels' transparency, tracers need to be added to the gels in order to perform both dynamic and structure experiments. In the case of the velocity profile measurements, carboxylated fluorescent colloids (Fluorescent Microspheres, Molecular Probes) of 1 μm diameter are added to the solution with a volume fraction of about $\phi = 2 \cdot 10^{-5}$ as described in [10]. In the case of the characterization of the gel structure, we mix 50 μL of a rhodamine B solution at 4 mM into 2 or 3 mL of Carbopol microgel already at $p\mathrm{H} = 7$. The dye is therefore used as a marker of the microgel structure. This protocol is actually inspired by the work of [37] where they used Acridine Orange dye to observe the structures of low-*p*H Carbopol. Note that for these low pHs, the polymer chains are not fully swollen and the jamming is not completed. As a benchmark experiment to check the influence of stirring on the gel structure [38], unstirred Carbopol gel at $C = 0.5$ %wt was also prepared. The results concerning this unstirred gel are shown and discussed in appendix B.

[1] The ratio between the elastic modulus G' and the yield stress σ_Y for pNipam microgel is typically two or three orders of magnitude higher than the one of Carbopol gels.

[2] This structure length will be defined as the equivalent of a particle diameter in other YSF (emulsions, foams, granular materials).

[3] The influence of the stirring on the structure is discussed in more details in sect. 3.2 and in appendix B.

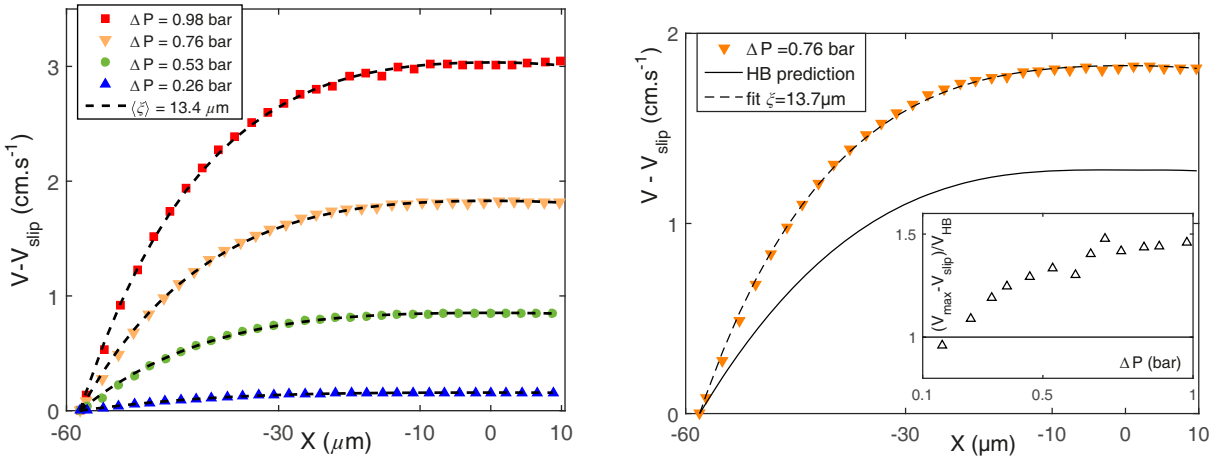

Fig. 1. Left: Velocity profiles measured in micro channel at several pressure drops for a 0.5 %wt Carbopol gel. The dashed lines are the fits by the fluidity model using a single cooperative lengthscale $\langle\xi\rangle = 13.4\,\mu$m. Right: HB prediction *vs.* experimental data. HB rheology fails to predict the confined velocity profile as the velocity profile predicted by the bulk rheology (plain line) is 40% smaller than the measured one (plain triangle). The velocity profile is well fitted by the fluidity model (dashed line) with a cooperative length of $\xi = 13.7\,\mu$m. Inset: ratio between the measured maximum flow velocities $V_{\max} - V_{\rm slip}$ and the maximum velocity expected by the bulk HB rheology $V_{\rm HB}$ as a function of the pressure drops.

Rheological measurement

The macroscopic flow curves are measured using a rheometer (Anton Paar MCR 301) with a rough Plate-Plate geometry to reduce slippage. Special care is taken to correct the stress inhomogeneities due to this geometry [10]. The gap between the two plates is fixed to 1 mm. The measured flow curves are well described by the phenomenological Herschel-Bulkley (HB) law defined as [39]

$$\begin{cases} \sigma = \sigma_Y + K\dot{\gamma}^n, & \text{if} \quad \sigma \geq \sigma_Y, \\ \dot{\gamma} = 0, & \text{if} \quad \sigma \leq \sigma_Y, \end{cases} \tag{1}$$

where σ is the applied shear stress, σ_Y the critical yield stress, K the consistency, $\dot{\gamma}$ the shear rate and n the HB exponent. For Carbopol gels, it has been shown [10] that the flow curves obtained at different gaps are all well described by a unique HB law as long as the gap is greater than 500 μm. In the following, we will refer to these measurements as *the "bulk"* rheology. Values of the HB parameters (σ_Y, K, n), for concentrations of Carbopol ETD 2050 ranging from $c = 0.25$ and 1 %wt, can be found in [10].

Velocity profiles measurement

Full details of the experimental procedure for the velocity measurements can be found in ref. [10], and only the main points are recalled here. Flows are performed in a large aspect ratio micro-channels ($w/h \ll 1$) where the width is $w = 116\,\mu$m, the height is $h = 1$ mm and total length is $L = 45$ mm. That way, flow profiles are essentially invariant along the height; velocities are measured in the middle plane $h/2$ far from edge effects. The experiments are driven at several fixed pressure drops ranging from $\Delta P = 0.1$ bar to $\Delta P = 1$ bar, which allow to explore a large range of shear stress σ up to 100 Pa. The tracers embedded in the gels are illuminated by laser pulses and a synchronized camera records their displacements in the channel. The processed movies are analysed with a particle tracking algorithm from which the particle velocities are obtained. Finally, the velocity profiles are obtained by a binning process over 2 μm steps across the channel width w. Note that we checked that profiles are insensitive to the binning details as soon as steps are below around 4 μm. As for the slip velocity, it is obtained by a linear extrapolation of the velocity profile at the wall position. With such procedures, the error bar on velocities are less than 1% [10]. Representative examples of velocity profiles are shown in fig. 1. Note that because of symmetry, the field of the camera was set to cover a bit more than the half of the channel —wall included—, so that only half velocity profiles are plotted.

2.2 Velocity profiles in confined geometries

Some velocity profiles were previously presented in [10] for 1 %wt Carbopol. Here, we briefly recall the different observations presenting data from different conditions, with 0.5 %wt Carbopol gels at different pressure drops. More precisely, fig. 1 (left) represents the difference $V - V_{\rm slip}$, between the local and the slip velocities, as a function of the position, X, in the micro-channel gap, with the origin set in the micro-channel center. Note that our experimental set-up allows to measure velocity up to a few cm/s thus giving access to relatively high shear rates. For a given driving pressure $\Delta P = 0.76$ bar, such a velocity profile is compared to the expected profile calculated from the known local shear stress and from the independently measured "bulk" rheology. Very clearly, prediction from

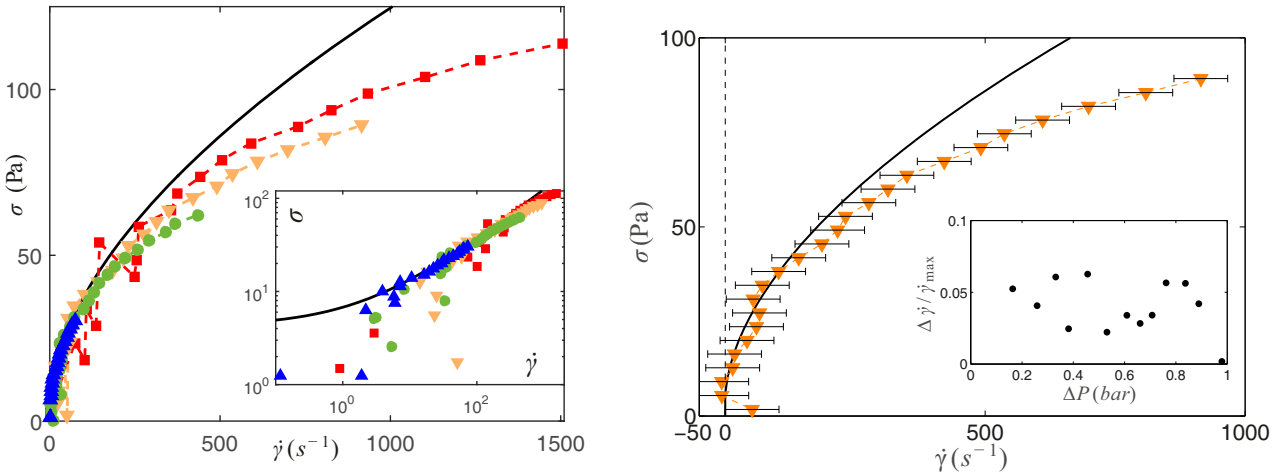

Fig. 2. Left: Local rheological curves computed from the velocity profiles of fig. 1 (left). The shear stresses σ are obtained by multiplying the positions X by the pressure drop $\Delta P/L$ and the shear rates from the derivation of the velocity profiles. The dashed lines are guides for the eye while the plain line corresponds to the bulk rheology. Inset: zoom on the local rheology at small shear rates in a log-log scale. Right: Local rheological curve computed from the velocity profile obtained at $\Delta P = 0.76$ bar including error bars on the local shear rate. The error bar on the shear rate is here $\Delta\dot{\gamma} = 50\,\mathrm{s}^{-1}$. The error bar on the shear stress is not significant and has not be plotted. The plain line corresponds to the bulk rheology. Inset: Relative error bars on the shear rate for all studied pressure drops. $\Delta\dot{\gamma}$ ranges from 0 to $50\,\mathrm{s}^{-1}$ and the maximum relative error is of 6%.

bulk behavior fails at accounting for the measurement, with a discrepancy of more than a factor 1.4 on maximum velocities values. As can be seen in the inset of fig. 1 (right), this departure from bulk predictions is observed for all pressure drops except the smallest one.

Overall, our experiments unambiguously show that bulk rheology cannot predict the velocity profiles measured in micro-channels, which by itself is a clear evidence of the existence of confinement effects. Note that such effects have been similarly observed with a 0.25 %wt Carbopol gel (not shown here) and a 1 %wt Carbopol gel [10].

2.3 Local rheology

The previous approach, that consists on comparing measured velocity profiles and predicted one from a given —bulk—rheology, is perfectly suited to evidence the confinement effects and the breakdown of a unique rheological law for the material. However, it is often preferred in the literature a method that consist in deducing a local rheology from the velocity profiles [9,31]. Here we perform such an analysis and discuss the limitations and drawbacks of the method.

In a bidimensional flow as approximated by our high aspect ratio, the local shear stress can just be obtained by multiplying the position X by the pressure drop, $\sigma = X(\Delta P/L)$. Because the corresponding local shear rate can be computed through derivation of the velocity profile ($\dot{\gamma} = \partial v/\partial X$), it is possible to compute a so-called local rheology law within the micro-channel as $\sigma[\dot{\gamma}(X)]$. Figure 2 (left) shows the local rheologies computed for the $C = 0.5$ %wt Carbopol gels flowing through the micro-channels at different pressure drops (see corresponding flow profiles in fig. 1 (left)) and fig. 2 (right) shows one local rheology obtained at $\Delta P = 0.76$ bar including error bars on the shear rate, here $\Delta\dot{\gamma} = 50\,\mathrm{s}^{-1}$. We choose this specific flow curve because it exhibits one of the highest error bars $\Delta\dot{\gamma}$ (see inset of fig. 2 (right)). First it appears that the measured local rheologies do not match the "bulk" one even if taking into account the highest error bar on the shear rate (see fig. 2 (right)). This result is in agreement with the previous claims from velocity profiles. Second, we evidence that not only there is a deviation to "bulk" behavior but there is not even a single rheological law as it is clear that local rheologies are dependent on the applied pressure ΔP, with no overlap obtained in their high shear rates portions. When focusing on small shear rates (inset of fig. 2 (left)), the data are more dispersed due to the small variations of the velocities in the channel center, amplified by the derivative computation. Nonetheless one can notice that shear rates are still measured for shear stresses smaller than the yield stress, which is consistent with simulation predictions in confined geometries [40].

Overall, the non-uniqueness of a flow curve for Carbopol gels in confined geometries constitutes a signature of non-local effects, which precludes a quantitative description of the liquids dynamics from bulk measurements. As evidenced though, deviations manifest more clearly for higher shear rates (here typically $\dot{\gamma} \geq 10^2\,\mathrm{s}^{-1}$). In a previous study on confined flows of N-isopropylacrylamide gel particles [31], a contradictory result was reported where local rheologies collapsed onto the bulk rheology thus leading to the conclusion of the absence of non-local effects. However, let us stress that this result was obtained for

shear rates below $10\,s^{-1}$; in view of our results on a much wider shear rate range, this might be quite insufficient to detect the effects of non-locality.

Finally, as for the two methods —comparing the measured and predicted velocities or the local and bulk rheologies— they both lead to the same conclusion: bulk rheology clearly fails to predict the behaviour of Carbopol gels in confined geometry due to non-local effects. However it is worthwhile to mention that the numerical derivative of the velocity profiles to calculate the local shear rate introduce experimental uncertainties, especially at small shear rates, so that comparing the velocity profiles is a more accurate method.

2.4 Cooperativity length

In order to rationalize the measured discrepancies between confined flow profiles and predicted one according to bulk rheology, we now consider the recently introduced fluidity model [9, 24, 40, 41]. This model relies on a cooperativity length ξ which corresponds to the range over which a rearrangement between polymer blobs impact their neighborhood. Such model has been previously used in ref. [10] to obtain ξ for Carbopol gels with different concentrations. We present here the specific results obtained with 0.5 %wt Carbopol gels.

Fluidity model ingredients

First, let us recall the main ideas of the fluidity model. The behavior of the fluid is described by a "fluidity" defined by the following constitutive relationship as

$$\dot{\gamma} = f[\sigma] \cdot \sigma. \tag{2}$$

The fluidity is homogeneous to the inverse of an effective viscosity and is proportional to the rate of plastic events occurring during the flow. Equation (2) is associated with the stationary non-local equation

$$\xi^2 \triangle f + f_b[\sigma] - f = 0, \tag{3}$$

in which appears the cooperativity length ξ as the characteristic distance over which the fluidity diffuses. In this equation, the term $f_b[\sigma(x)]$ stands for the bulk fluidity obtained with eq. (2) and the bulk rheology (HB, eq. (1))

$$\begin{aligned} f_b[\sigma] &= \frac{1}{\sigma}\left(\frac{\sigma-\sigma_Y}{K}\right)^{1/n}, \quad \text{if } \sigma > \sigma_Y, \\ &= 0 \quad \text{otherwise.} \end{aligned}$$

Note that there is no contradiction between the bulk rheology (HB) and the fluidity model: at large scales, *i.e.* for channel sizes much larger than ξ, the Laplacian contribution in eq. (3) becomes negligible compared to the other term. The bulk behavior is then recovered $f = f_b$. At shorter scales, this description introduces a microscopic ingredient ξ which enables to understand the fluid dynamic. In this description, the bulk rheology is then an asymptotic behavior of the fluid at macroscopic scales.

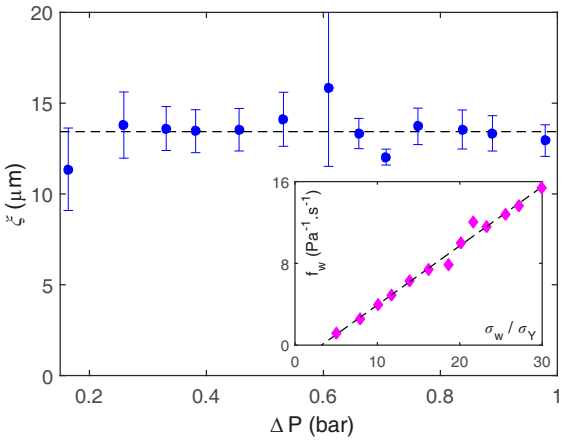

Fig. 3. Cooperativity lengths ξ, with associated error bars, measured at several pressure drops ΔP (blue dots) and their mean value (dashed line). Inset: Wall fluidity f_w extracted from the velocity profiles at several pressure drops, converted in wall shear stress σ_w. The wall fluidity presents a linear dependence (red line) in σ_w and vanishes to 0 for a shear stress greater than σ_Y, the bulk yield stress: $f_w = 0.58(\sigma/\sigma_Y - 3.21)\,\mathrm{Pa}^{-1}\,\mathrm{s}^{-1}$.

Cooperativity length and wall fluidity measurements

Equation (3) can be simplified in our geometry since the flow is 2D, and all variables only depend on the transverse coordinate X. The stress field $\sigma(X)$ being fixed by the pressure drop $\Delta P/L$, eq. (3) can be solved across the channel [10]. Integrating eq. (2) with the corresponding solution $f(X)$ allows to compute the velocity profiles

$$v(X, \xi, f_w) = \int_{-w}^{X} f(\sigma(x'), \xi, f_w) \cdot \sigma(x') \mathrm{d}x'. \tag{4}$$

The velocity profiles eventually depend on two parameters, ξ and f_w. The latter stands for the wall fluidity which is fixed by the boundary conditions $f_w = f(\pm X_{\mathrm{wall}}) = \dot{\gamma}_w/\sigma_w$. Equation (4) is hard to compute analytically given the expression of $f(X)$. Nonetheless it can be integrated numerically to fit the velocity profiles with the two parameters[4] ξ and f_w.

Inset of fig. 3 shows the wall fluidity f_w obtained for several pressure drops. The linear dependence of the wall fluidity with the wall shear stress has also been observed in confined flows of dense emulsions [20], but the cancellation for a non-zero wall shear stress is not yet understood. This could be due to a specific behavior of the fluid near the walls, similar to flow structuration in emulsions, that we can not evidence with our device. Figure 3 shows the cooperative length ξ obtained for several pressure drops. The cooperativity length is found essentially independent on the imposed pressure drop: the average value $\langle\xi\rangle$ is thus used as a unique characteristic to compute velocity profiles from the fluidity model. As shown in fig. 1 (left),

[4] The wall fluidity is indeed kept as a free parameter because of the existence of the slip velocity which does not allow to estimate the wall shear rate precisely enough.

this single property $\langle\xi\rangle = 13.4\,\mu$m successfully captures the confined dynamics of $C = 0.5\,\%$wt Carbopol gels for all experimental conditions.

Now to proceed in the understanding of the relationship between microscopic material properties and dynamical behavior requires some insights into the structural features that characterize Carbopol entangled polymer gels. Indeed, the consistency of the fluidity approach involves that the cooperativity length be associated to an underlying structure size D with typical ranges from $\xi/D \sim 1$–10.

3 Carbopol microstructure studied by confocal microscopy

As mentioned in the introduction, Carbopol gels are composed of highly cross-linked polymers swollen in water with a chemical base; the swelling of the polymer blobs inducing the jamming of the whole structure. Although some characterizations of the gel structure has been performed with small angles light scattering [36], they proved difficult because of the high material transparency. Moreover, they demonstrated a strong sensitivity to preparation protocol so that accurate confrontation of structural and dynamical results require comparing identically prepared samples. Here we propose an original and simple method based on confocal microscopy and image correlation spectroscopy (ICS) to access the characteristic structure length scale in Carbopol gels, in order to discuss its relationship with previously determined flow properties.

3.1 Material and methods

Image acquisition

The structure of carbopol gels are observed with a confocal microscope (Leica). Drops of Carbopol gels labelled with Rhodamine B are deposited on a glass slide and examined with dry objective (20× magnification, NA = 0.70). HeNe laser ($\lambda = 543$ nm) is used for illumination with collected fluorescence bandwidth set to [552 nm–692 nm]. Line and frame averaging during image acquisition are set respectively to 10 and 16.

Structure observation

A typical observation of the gel structure is shown in fig. 4. Unlike images from emulsions, foams or granular materials, it is clear that no elementary particle can be identified. Nonetheless the image exhibits noticeable spatial intensity variations associated with a cloudy structure made of grey patches whose typical size will be examined in the next section. As previously proposed [37] the fluorescent contrast in the images comes from the preferential enhancement of dye concentration in polymer rich region due to interactions with the polymer backbone either associated to borne charges or hydrophobicity. Therefore fluorescence intensity unveils the heterogeneity in polymer distribution. Besides the overall space-filling cloudy structure compatible with the jammed blob structure, one can distinguish few voids in the structure —under the form of dark regions— together with sparse bright spots indicating very dense polymer regions (see figs. 4, 6). These small and dense regions are reminiscent of previous work on the Carbopol structure [36]. Although their size is here nearly resolution-limited, it appears in agreement with the few hundreds of nanometers length scales already reported [36] (see appendix A for more details). We now turn to the analysis of the main structural element: the space-filling cloudy structure.

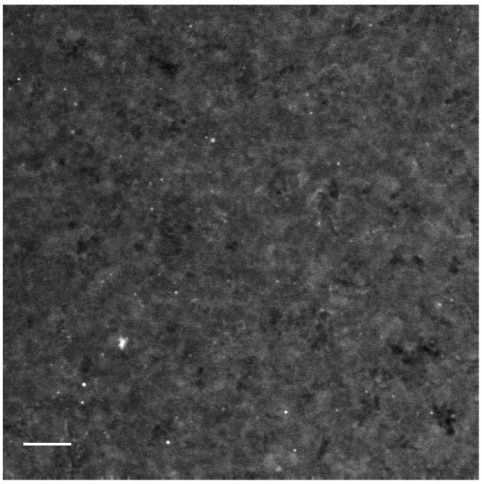

Fig. 4. Structure of a 0.5 %wt Carbopol gel: fluorescent image of the gels labelled with Rhodamine B. The picture dimensions are $101 \times 101\,\mu$m^2 and the length of the white bar is $10\,\mu$m.

3.2 Structure size measurements

Image correlation spectroscopy

Extraction of the gel structural features is performed using a Intensity Correlation Spectroscopy (ICS) approach, mostly developed in biological imaging context. This analysis is based on the calculation of the autocorrelation functions of the images intensity i [42, 43]. The normalized intensity fluctuations are defined as

$$\delta i(x', y') = \frac{i(x', y') - \langle i\rangle}{\langle i\rangle}\,, \tag{5}$$

with $i(x', y')$ the fluorescence intensity of the (x', y') pixel and $\langle i\rangle$ the average value over the whole image. The normalized correlation function $g(x, y)$ is then defined as

$$g(x, y) = \langle \delta i(x', y')\delta i(x' + x, y' + y)\rangle. \tag{6}$$

Developing eq. (6) with eq. (5) allows to express g as a function of the raw image autocorrelation function $G(x, y) = \langle i(x', y')i(x' + x, y' + y)\rangle$

$$g(x, y) = \frac{G(x, y)}{\langle i\rangle^2} - 1.$$

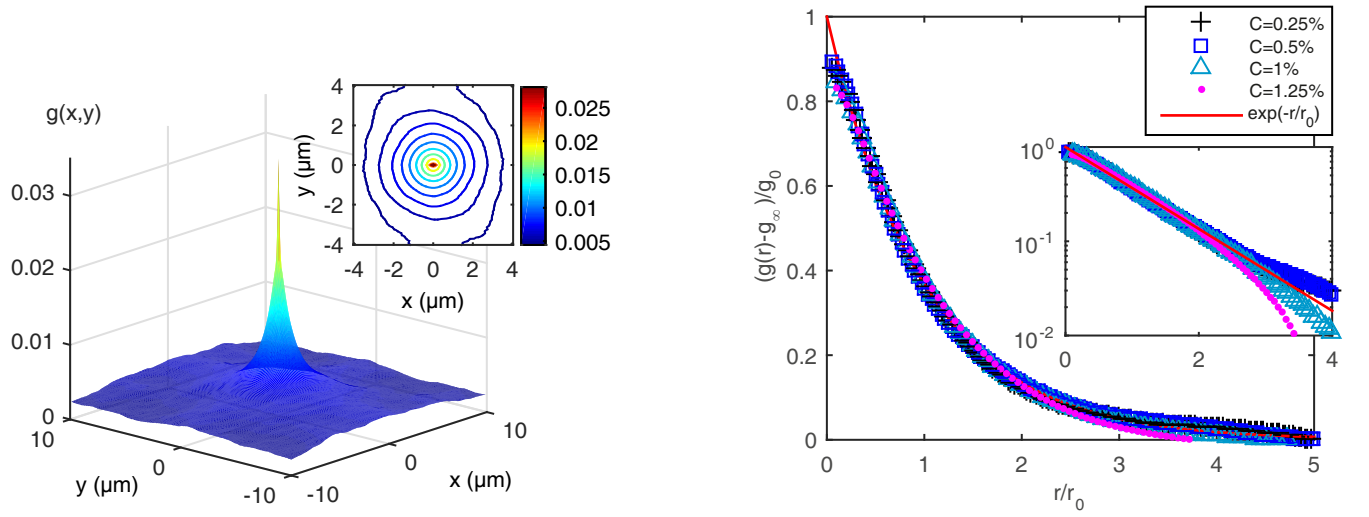

Fig. 5. Left: Representation of normalized autocorrelation function $g(x, y)$ from intensity fluctuations as found from fig. 4. Inset: contour plots in the peak vicinity showing radial symmetry. Right: Radial correlation functions in non-dimensionalized coordinates for different samples with concentration from 0.25 to 1.25 %wt, showing good collapse onto a single exponential decay. Inset: same in a log-log scale.

Practically, $G(x, y)$ is computed by Fast Fourier Transforms (FFT) according to

$$g(x,y) = \frac{\mathcal{F}^{-1}[|\mathcal{F}[i]|^2]}{N_p\langle i\rangle^2}(x,y) - 1, \tag{7}$$

where the operators $\mathcal{F}[\cdot]$ and $\mathcal{F}^{-1}[\cdot]$, respectively, stand for the FFT and the inverse FFT, and where N_p is the total number of pixels of the images (here 1024^2). Note that due to the linearity of the fluorescence intensity with the dye concentration, $g(x, y)$ directly corresponds to the dye concentration fluctuation spatial autocorrelation function. With inhomogeneities associated with dye concentration enhancement due to the underlying polymer concentration [37], we further assume $g(x, y)$ to yield a good estimate of the polymer concentration autocorrelation function.

Correlation functions and size measurements

A typical autocorrelation function is shown fig. 5 (left) for a 0.5 %wt Carbopol sample, representative of all samples and concentrations analyzed. A sharp correlation peak is present, essentially isotropic as can be seen (fig. 5 (left), inset), whose amplitude quickly decreases with the radial coordinate r. This correlation relaxation $g(r)$ is presented in fig. 5 (right), where we found that the function obeys an exponential decay (inset), consistent with the exponential decrease of the correlation function expected in semi-dilute polymer solutions [44]. Accordingly, $g(r)$ is fitted by

$$g(r) = g_0 \exp\left(-\frac{r}{r_0}\right) + g_\infty, \tag{8}$$

where the correlation length r_0 stands for an equivalent particle radius, and with g_0 and g_∞ the peak intensity and the correlation background respectively[5]. Note that because $g(r = 0)$ value gathers contribution from all uncorrelated noise sources, its value is treated as a free parameter in the fitting process [42] from which the $r = 0$ data are excluded. Performing this ICS analysis for different samples and different concentrations, we verify that the exponential decay of the correlation is well obeyed throughout all our experimental conditions (fig. 5 (right)). This allows us to provide an equivalent particle diameter or structure size $D = \langle 2r_0\rangle$ for the different polymer concentrations, which are summarized in table 1. Additionally, note that the effect of the preparation protocol is also reported (see appendix B).

Table 1. Summary table of the different parameters measured by fitting the data using eq. (8) for Carbopol gels. Variables C and $D = 2r_0$ are, respectively, the polymer weight concentration and the average structure size with associated standard errors. $\langle g_0\rangle$ is the average peak amplitude, while N is the number of samples analyzed for each preparation.

C (%wt)	$D = 2r_0$ (μm)	$\langle g_0\rangle$	N
0.25%	3.4 ± 0.4	$3.2\,10^{-2} \pm 0.4\,10^{-2}$	10
0.50%	3.0 ± 0.3	$6.6\,10^{-2} \pm 1.1\,10^{-2}$	10
1%	2.4 ± 0.1	$1.0\,10^{-1} \pm 1.2\,10^{-2}$	10
1.25%	2.2 ± 0.1	$1.3\,10^{-1} \pm 0.6\,10^{-2}$	10

Examining the reported structure sizes, several results emerge. First, the average structure size of Carbopol gels is in the range 2–4 microns. This typical size is in good agreement with the previous study [36] that used small angles light scattering measurements. Indeed, it reported structure sizes ranging from 1 to 10 μm depending on the preparation protocol. Note that the interpretation of scattering experiments also involved the introduction of an ad-

[5] Typically $\langle g_\infty\rangle$ is one order smaller than $\langle g_0\rangle$.

Table 2. Summary table of the different characteristic lengths with standard errors: $\langle\xi\rangle$ and D, respectively, stand for the cooperative length and the structure size and C corresponds to the Carbopol weight concentration.

C (%wt)	$\langle\xi\rangle$ (μm)	D (μm)	$\langle\xi\rangle/D$
0.25%	7.3 ± 1.2	3.4 ± 0.4	2.1
0.50%	13.4 ± 0.6	3.0 ± 0.3	4.5
1%	11.7 ± 0.9	2.4 ± 0.1	4.9

ditional, submicrometric second length scale. We provide additional information on both the effect of the preparation protocol and the origin of the second length scale in appendices A and B. Essentially, unstirred samples are found more heterogeneous, and with a bigger characteristic size ($D \sim 6\,\mu$m), in good agreement with previous rheological studies [38].

Coming back to the results summarized in table 1, the second result evidenced is the decrease of the structure size D with the increase of the polymer concentration. Intuitively, this can be explained by the fact that polymer blobs are more compressed when the concentration goes up. In the framework of polymer physics, it is also well-known that the characteristic length between the entanglements in semi-dilute solution of polymer decreases as the concentration increases [44].

Overall, the simple imaging and analyzing method presented here proves very efficient to yield direct access to the gel structural characteristics, which could only be hinted at so far by a single and much more demanding small-angles light-scattering experiment [36].

3.3 Length scales comparison

The structure sizes can now be compared to the cooperative lengths measured in sect. 2 on stirred Carbopol gel. In particular, for a 0.5 %wt Carbopol gel, the velocity profile adjustments shown in fig. 3 correspond to an average cooperativity length of $\langle\xi\rangle = 13.4\,\mu$m. For the same Carbopol concentration, the characteristic structure size found from ICS is $D = 3.6\,\mu$m so that the cooperativity length $\langle\xi\rangle$ corresponds to about 4 polymer blobs. This is fully consistent with the underlying microscopic picture for ξ in the frame of fluidity model or in the frame STZ descriptions.

Similar analysis have been performed with two other polymer concentrations: 0.25 %wt (not shown here) and 1 %wt Carbopol gels [10]. The comparison between cooperative lengths and structure sizes is summarized in table 2. For all concentrations, the cooperative length is of the order of a few polymer blobs (from 2 to 5). More precisely the ratio $\langle\xi\rangle/D$ is around 2 for the lowest used polymer concentration (0.25 %wt) —*i.e.* for the softer gel and thus the largest structural size D— and this ratio increases monotonically with the polymer concentration. Overall, we found that the harder the system, the more cooperatively it behaves. Note that this trend could not be predicted by the unique knowledge of the cooperative length $\langle\xi\rangle$ which has to be normalized by the structure size.

To conclude, the length scale measured in the frame of the fluidity model actually corresponds to a range over which a few gel microstructures flow cooperatively. These observations also join the STZ description for the flow of complex fluids and give a new insight into the understanding of the behavior of entangled polymer gels at microscopic scales.

4 Conclusions

In this paper, we report for the first time the dual measurement of structural lengths and cooperativity lengths under confined flow, for a highly entangled polymer gel. Using Carbopol as a model Yield Stress Fluid, we first measured velocity profiles in micro-channels, thus demonstrating strong deviations from the bulk rheological behavior of the material. Experiments were carefully analyzed in terms of both theoretical velocity profiles or local rheology measurements, showing non-local effects at high shear rates $\dot{\gamma} \geq 10^2\,\mathrm{s}^{-1}$. In an experimental perspective, we showed that such access to high shear rates appears as an important methodological feature as lower shear rates alone could lead to erroneous conclusion with respect to confinement effects.

The further analysis of the measured velocity profiles within the framework of the fluidity model allows to fully rationalize our observations and to measure a unique cooperativity length scale of the order of $\langle\xi\rangle \simeq 13\,\mu$m for stirred 0.5 %wt Carbopol gels under all driving pressure conditions.

Complementarily, we proposed a simple and original method to observe the microstructure of Carbopol gels by fluorescence confocal imaging of dye-loaded swollen gel's particles. The analysis based on Image Correlation Spectroscopy yielded structure characteristics which support the general outcomes from the only previous small-angles light-scattering experiment performed on Carbopol ETD 2050 microgels [36]. Polymer gel structural sizes are essentially in the 1–10 μm range with a dependency on the preparation —stirring here— protocol. More precisely in our case polymer concentration dependency is noticeable but weak, and the typical structural size D of all stirred sampled is typically around 3 μm.

Comparing the two length scales precludes any confusion between the cooperativity length and the gels structure sizes for all the polymer concentrations of stirred Carbopols: the cooperative length is always of the order of several structure sizes. Overall, this study provides a clear demonstration of the still-debated soundness of the fluidity model and Shear Transition Zone picture for highly entangled polymer gels. However, it should be stressed that many open questions still remain for a complete comprehensive relationship between microscopic structural and dynamic features and global response of yield stress materials. This is especially true for processes occurring near the confining solid walls. Indeed the fluidization mechanism near the walls is still misunderstood while it appears

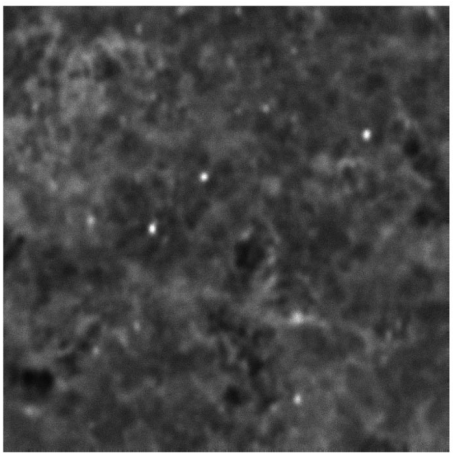

Fig. 6. Magnification of the small structures (bright spots) observed in a stirred 0.5 %wt Carbopol. The image is obtained by cumulating 50 frames with 10 accumulations per line with a confocal microscope. The dimensions of the image are $24.6 \times 24.6\,\mu\text{m}^2$. The characteristic size of the small structures (white spots) is $0.5\,\mu$m.

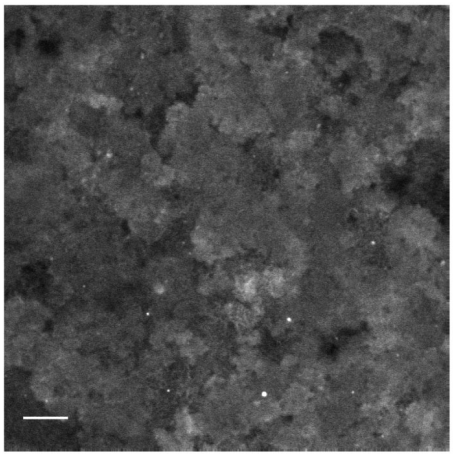

Fig. 7. Structures of an unstirred 0.5 %wt Carbopol. The picture dimensions are $101\,\mu\text{m} \times 101\,\mu$m and the white bars corresponds to $10\,\mu$m.

to drive the whole flow. An interesting direction would be to probe the influence of slippage on the results by tuning the affinity of the walls for the gels as shown in a recent study [45]. The relationship between the wall roughness, the wall slip and the wall fluidity now appears as one of the most important rationalization step that we plan to address in future studies.

We thank N. Louvet for helping us with the fabrication of the microchannels. We thank L. Bocquet, A. Colin, J. Goyon, B. Dollet and A. L. Vayssade for enlightening discussions. We acknowledge support from the ANR, through the program ANR Blanche (Maniphyc) and from the institut universitaire de France (IUF).

Appendix A. Carbopol structures

Using light scattering experiments at small angles, Lee *et al.* [36] have revealed the existence of two characteristic length scales in the microstructure of Carbopol ETD 2050 microgel: a large one of few microns that depends on the polymer concentration and the *p*H and a small one of 400 nm independent of those parameters. This small structure was interpreted as a dense region of unswollen polymers.

Indeed, our direct imaging method allows an easy observation of such features as can be seen in fig. 6 where small and sparse bright spots appear in top of the global cloudy structure. Analyzing the intensity profile of these bright features, they appear of typical size around $0.5\,\mu$m. With a confocal lateral resolution of $0.3\,\mu$m in our conditions, the physical size of these bright feature is thus around a few hundreds nanometers. This is in good agreement with the small-size population that was introduced to analyze scattering results. Although no definite conclusion can be drawn from the only images, they likely correspond to unswollen/undissolved aggregates. More than the size or the nature of these aggregates, the main point arising from the images however is that these small-size feature are marginal and unlikely of any relevance for the fluids properties. Overall, the structure of Carbopol gels can be seen as a set of soft polymer blobs of the microns scale with very few small aggregates.

Appendix B. Unstirred Carbopol gels microstructure

The influence of the preparation protocol on the Carbopol microstructure is presented in this appendix. More precisely, the structure of an unstirred Carbopol is studied and compared to the one of a stirred Carbopol at the same concentration $C = 0.5\,\%$wt.

Appendix B.1. Structure sizes

A typical image of unstirred Carbopol gel is shown in fig. 7. Comparing figs. 4 and 7 shows that the unstirred Carbopol exhibits bigger structures than the stirred one. To be more quantitative, the same ICS analysis can be performed. The correlation functions obtained with unstirred samples also present a radial symmetry but they are not so well-fitted by eq. (8). A better fitting model is given by

$$g(r) = g_0 \exp\left(-(r/r_0)^\alpha\right) + g_\infty,$$

where $\alpha \approx 0.7$ in our measurements. An interesting point here is the value of α, below 1, which could be the signature of a slightly different structure with long-range correlations. The equivalent particle size is however of the same order of magnitude of a few microns. More precisely, for unstirred Carbopol, $\langle D \rangle = 6.2 \pm 1.1\,\mu$m which is twice the structure size of a stirred Carbopol gel at the same concentration ($c = 0.5\,\%$wt).

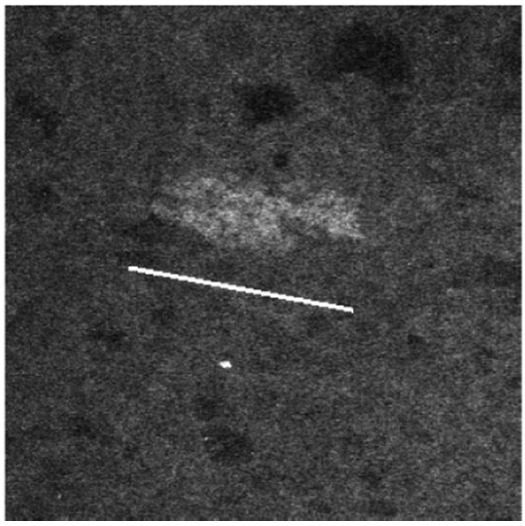

Fig. 8. Huge polymer cluster in an unstirred 0.5 %wt Carbopol. The dimensions of the picture are $294\,\mu\text{m} \times 294\,\mu\text{m}$ and the size of the white bar is $130\,\mu\text{m}$.

Appendix B.2. Heterogeneous structure

The second feature that we want to stress here concerns the existence of huge clusters among the structure of unstirred Carbopol gels. An example of such clusters, whose sizes are of the order of $100\,\mu\text{m}$, is provided in fig. 8. The presence of such clusters in the samples can be explained by the fast swelling of the entangled structures during the addition of the chemical base. The presence of these clusters actually confirms the assumption formulated to explain the flow reduction reported with unstirred Carbopols in ref. [10], since their size is comparable to the channel's width.

References

1. R.G. Larson, *The Structure and Rheology of Complex Fluids* (Oxford University Press, 1999).
2. S.A. Rogers, D. Vlassopoulos, P.T. Callaghan, Phys. Rev. Lett. **100**, 128304 (2008).
3. M. Le Merrer, S. Cohen-Addad, R. Höhler, Phys. Rev. Lett. **108**, 188301 (2012).
4. E.D. Knowlton, D.J. Pine, L. Cipelletti, Soft Matter **10**, 6931 (2014).
5. P.C.F. Möller, S. Rodts, M.A.J. Michels, D. Bonn, Phys. Rev. E **77**, 041507 (2008).
6. R. Besseling, L. Isa, P. Ballesta, G. Petekidis, M.E. Cates, W.C.K. Poon, Phys. Rev. Lett. **105**, 268301 (2010).
7. W.K. Kegel, A. van Blaaderen, Science **287**, 290 (2000).
8. S.P. Meeker, R.T. Bonnecaze, M. Cloitre, J. Rheol. **48**, 6 (2004).
9. J. Goyon, A. Colin, G. Ovarlez, A. Ajdari, L. Bocquet, Nature **454**, 84 (2008).
10. B. Géraud, L. Bocquet, C. Barentin, Eur. Phys. J. E **36**, 13030 (2013).
11. G.C. Maitland, Curr. Opin. Colloid Interface Sci. **5**, 301 (2000).
12. A. Cuenca, H. Bodiguel, Phys. Rev. Lett. **108**, 108304 (2013).
13. A. Muggeridge, A. Cockin, K. Webb, H. Frampton, I. Collins, T. Moulds, P. Salino, Philos. Trans. R. Soc. London A: Math. Phys. Eng. Sci. **372**, 2006 (2013).
14. A. Argon, Acta. Metall. **27**, 47 (1979).
15. V.V. Bulatov, A. Argon, Model. Simul. Mater. Sci. Eng. **2**, 167 (1994).
16. P. Olsson, S. Teitel, Phys. Rev. Lett. **99**, 178001 (2007).
17. A. Lemaître, C. Caroli, Phys. Rev. Lett. **103**, 065501 (2009).
18. P. Schall, D.A. Weitz, F. Spaepen, Science **318**, 1895 (2007).
19. P. Jop, V. Mansard, P. Chaudhuri, L. Bocquet, A. Colin, Phys. Rev. Lett. **108**, 148301 (2012).
20. V. Mansard, L. Bocquet, A. Colin, Soft Matter **10**, 6984 (2014).
21. K.N. Nordstrom, J.P. Gollub, D.J. Durian, Phys. Rev. E **84**, 021403 (2011).
22. P. Chaudhuri, V. Mansard, A. Colin, L. Bocquet, Phys. Rev. Lett. **109**, 0360001 (2012).
23. A. Nicolas, J.L. Barrat, Phys. Rev. Lett. **110**, 138304 (2013).
24. J. Goyon, A. Colin, G. Ovarlez, A. Ajdari, L. Bocquet, Soft Matter **6**, 2668 (2010).
25. K.A. Reddy, Y. Forterre, O. Pouliquen, Phys. Rev. Lett. **106**, 108301 (2011).
26. K. Kamrin, G. Koval, Phys. Rev. Lett. **108**, 178301 (2012).
27. Benjamin Dollet, J. Rheol. **54**, 741 (2010).
28. B. Dollet, A. Scagliarini, M. Sbragaglia, J. Fluid Mech. **766**, 556 (2015).
29. A. Scagliarini, B. Dollet, M. Sbragaglia, Colloids Surf. A: Physicochem. Eng. Aspects **473**, 133 (2015).
30. R. Lespiat, S. Cohen-Addad, R. Höhler, Phys. Rev. Lett. **106**, 148302 (2011).
31. K.N. Nordstrom, J.P. Gollub, D.J. Durian, Phys. Rev. Lett. **105**, 175701 (2010).
32. Lubrizol pharmaceutical bulletins, Technical report, Lubrizol Corporation (2002).
33. P. Möller, A. Fall, V. Chikkadi, D. Derks, D. Bonn, Philos. Trans. R. Soc. A **367**, 5139 (2009).
34. M. Muramatsu, K. Kanada, A. Nishida, K. Ouchi, N. Saito, M. Yoshida, A. Shimoaka, T. Ozeki, H. Yuasa, Y. Kanaya, Int. J. Pharm. **199**, 77 (2000).
35. T. Divoux, D. Tamarii, C. Barentin, S. Teitel, S. Manneville, Soft Matter **8**, 4151 (2012).
36. D. Lee, I.A. Gutowski, A.E. Bailey, L. Rubatat, J.R. de Bruyn, B.J. Frisken, Phys. Rev. E **83**, 031401 (2011).
37. I.A. Gutowski, D. Lee, J.R. de Bruyn, B.J. Frisken, Rheol. Acta **51**, 441 (2012).
38. L. Baudonnet, J.L. Grossiord, F. Rodriguez, J. Dispersion Sci. Technol. **25**, 183 (2004).
39. W.H. Herschel, R. Bulkley, Kolloid-Zeitschrift **39**, 291 (1926).
40. V. Mansard, A. Colin, P. Chaudhuri, L. Bocquet, Soft Matter **9**, 7489 (2013).
41. L. Bocquet, A. Colin, A. Ajdari, Phys. Rev. Lett. **103**, 036001 (2009).
42. N.O. Petersen, P.L. Höddelius, P.W. Wiseman, O. Seger, K.-E. Magnusson, Biophys. J. **65**, 1135 (1993).
43. P.W. Wiseman, F. Capani, J.A. Squier, M.E. Martone, J. Microsc. **205**, 177 (2002).
44. M. Doi, S.F. Edwards, *The Theory of Polymer Dynamics* (Oxford Science Publications, 1988).
45. A.-L. Vayssade, C. Lee, E. Terriac, F. Monti, M. Cloitre, P. Tabeling, Phys. Rev. E **89**, 052309 (2014).